small
NANO MICRO
www.small-journal.com

Photoassisted Construction of Holey Defective g-C_3N_4 Photocatalysts for Efficient Visible-Light-Driven H_2O_2 Production

*Li Shi, Liuqing Yang, Wei Zhou, Yanyu Liu, Lisha Yin, Xiao Hai, Hui Song, and Jinhua Ye**

Holey defective g-C_3N_4 photocatalysts, which are easily prepared via a novel photoassisted heating process, are reported. The photoassisted treatment not only helps to create abundant holes, endowing g-C_3N_4 with more exposed catalytic active sites and crossplane diffusion channels to shorten the diffusion distance of both reactants from the surface to bulk and charge carriers from the bulk to surface, but also introduces nitrogen vacancies in the tri-s-triazine repeating units of g-C_3N_4, inducing the narrowing of intrinsic bandgap and the formation of defect states within bandgap to extend the visible-light absorption range and suppress the radiative electron–hole recombination. As a result, the holey defective g-C_3N_4 photocatalysts show much higher photocatalytic activity for H_2O_2 production with optimized enhancement up to ten times higher than pristine bulk g-C_3N_4. The newly developed synthetic strategy adopted here enables the sufficient utilization of solar energy and shows rather promising for the modification of other materials for efficient energy-related applications.

1. Introduction

Hydrogen peroxide (H_2O_2) has attracted much attention as an ideal energy carrier alternative to hydrogen, because it is soluble in water and can be used in a one-compartment fuel cell to generate electricity.[1,2] Semiconductor photocatalysis is regarded as one of promising technologies for H_2O_2 synthesis, due to the safe and energy-saving properties.[3–5] In the photocatalytic process, H_2O_2 can be produced via two-electron reduction of O_2 by the conduction band (CB) electrons from photoexcited semiconductor materials.[3] Currently, numerous research studies have mainly focused on the search and construction of highly efficient photocatalysts for energy-related applications.[6–8] Among various photocatalysts investigated, graphitic carbon nitride (g-C_3N_4) has stimulated tremendous research interest, mainly due to its unique features, such as suitable bandgap for visible light absorption, proper band edges for target reactions, environmental benignity, fairly good thermal and chemical stability, and cost effective metal-free composition.[9–16] Up to now, g-C_3N_4 has achieved good photocatalytic performances in many kinds of photocatalytic areas, such as H_2/O_2 evolution from water splitting, organic pollutant photodecomposition, and CO_2 reduction.[11,17–24] Recent works also indicated that g-C_3N_4 with suitable bandgap and band edge position could promote efficient two-electron reduction of O_2 to produce H_2O_2 under visible light irradiation.[25–28]

Bulk g-C_3N_4 (BCN) has limited visible-light absorption ability and also suffers from a low separation efficiency of photoexcited charge carriers, resulting in low photocatalytic activity.[29] Aiming at improving the photocatalytic performance of g-C_3N_4, various strategies have been developed, such as heteroatoms doping,[30,31] nanostructure design,[32–35] dye sensitization,[36,37] and coupling with other semiconductors or conductors.[38–41] Particularly, the introduction of nitrogen defects into the g-C_3N_4 framework was recently developed as an effective strategy to significantly enhance the photocatalytic activity of g-C_3N_4 under visible light.[42–45] The introduction of nitrogen defects in the tri-s-triazine repeating units of g-C_3N_4 can not only modify the electronic structure by narrowing the bandgap to promote more visible light harvesting, but also act as specific reactive sites for photocatalytic reactions.[42] The

Dr. L. Shi, Dr. X. Hai, H. Song, Prof. J. Ye
Graduate School of Chemical Sciences and Engineering
Hokkaido University
Sapporo 060-0814, Japan
E-mail: Jinhua.YE@nims.go.jp
Dr. L. Shi, L. Yang, Dr. L. Yin, Dr. X. Hai, H. Song, Prof. J. Ye
International Center for Materials Nanoarchitectonics (WPI-MANA)
National Institute for Materials Science (NIMS)
1-1 Namiki, Tsukuba, Ibaraki 305-0044, Japan
Prof. W. Zhou, Y. Liu
Department of Applied Physics
Tianjin Key Laboratory of Low Dimensional Materials Physics and Preparing Technology
Faculty of Science
Tianjin University
Tianjin 300072, P. R. China
Prof. J. Ye
TU-NIMS Joint Research Center
School of Materials Science and Engineering
Tianjin University
92 Weijin Road, Nankai District, Tianjin 300072, P. R. China
Prof. J. Ye
Collaborative Innovation Center of Chemical Science and Engineering
Tianjin 300072, P. R. China
The ORCID identification number(s) for the author(s) of this article can be found under https://doi.org/10.1002/smll.201703142.

DOI: 10.1002/smll.201703142

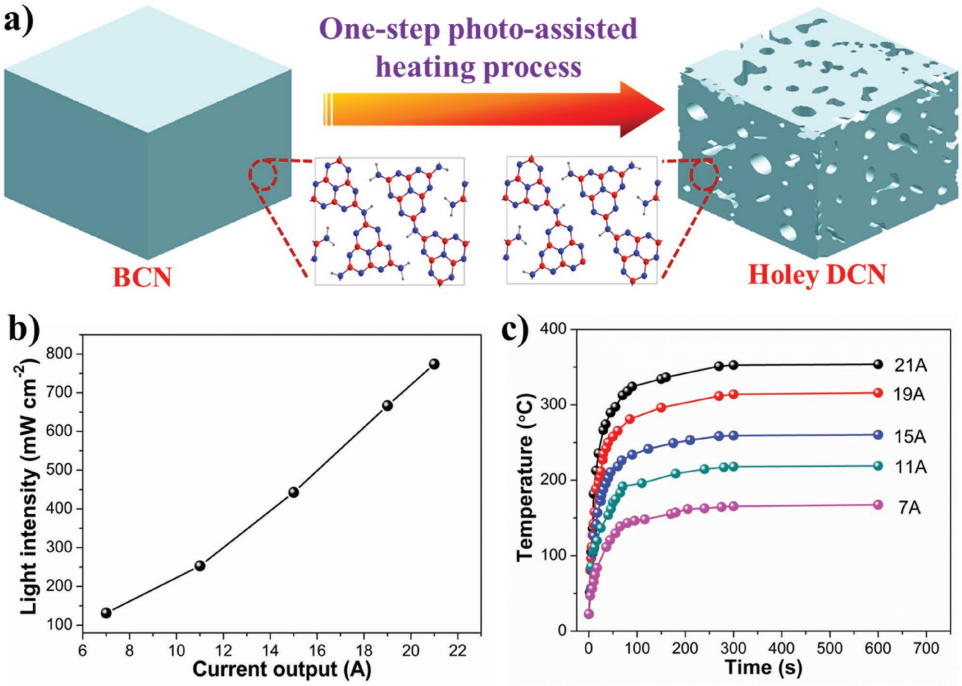

Figure 1. a) Illustration of the preparation process of holey DCN, and the insets are their simulated structure (H, C, and N atoms are represented by the gray, red, and blue balls). b) The relationship between light intensity and current output; c) the increase in temperature of g-C_3N_4 under light irradiation at different current output.

positive role of nitrogen defects in affecting the photocatalytic activities of g-C_3N_4 for H_2 evolution and organic molecular degradation has been actively reported, but rare for H_2O_2 production. What is more, approaches used to date for the introduction of nitrogen defects in g-C_3N_4 frameworks are usually based on the solid-state thermal polymerization or hydrothermal process heated at high temperature in an electric furnace in the presence of reducing atmosphere, which have inherent drawbacks such as high energy consumption.[45–47] Therefore, it is desirable to explore more facile and efficient approaches toward the construction of nitrogen defective g-C_3N_4 (DCN).

The recently emerged rapid heating of materials by photon energy[48] inspired us to seek new methods for preparing modified g-C_3N_4. In this work, we describe a novel one-step photoassisted route to prepare holey DCN by using hydrazine as a reducing agent (**Figure 1**a). In sharp contrast to the conventional approaches based on heating in an electric furnace, the photoassisted approach enables the rapid heating of materials within few minutes owing to the remarkable and prompt increase in the local temperature of materials under light irradiation. The introduction of nitrogen defects in g-C_3N_4 can not only narrow its intrinsic bandgap, but also create abundant defect states within bandgap, greatly increasing the visible-light absorption range and suppressing radiative electron–hole recombination. Moreover, holey structure can be built after this photoassisted reduction process, which allows for exposing more active sites and facilitates the accessibility of reactants to the active surface. As a result, the holey DCN shows much improved photocatalytic activity for H_2O_2 production than pristine BCN.

2. Results and Discussion

Direct irradiation of the BCN sample with hydrazine by a 300 W Xe lamp (the current outputs are set from 7 to 21 A) can produce DCN (χ A; χ indicates the current output). The light intensity of Xe lamp can be controlled by adjusting the current output (Figure 1b). The changes in temperature of BCN powder upon light irradiation at different intensities are depicted in Figure 1c. As can be seen, upon light irradiation, an instant and remarkable increase in the temperature of sample was observed (reaching the maximum temperature within only about 5 min). The fast and controllable photoassisted treatment enables the heating of g-C_3N_4 within few minutes, showing a desirable and effective synthetic approach for the modification of g-C_3N_4. At a light intensity of 774 mW cm^{-2} (full arc with a maximum input power of 300 W), the temperature of BCN reaches up to 350 °C. The good photothermal property of BCN indicates its efficient utilization of light energy. Under such high temperature, hydrazine can be evaporated, and also some part of hydrazine can be decomposed into reductive products NH_3 and H_2 according to the reaction equation (Equation S1, Supporting Information). The formation of NH_3 and H_2 can be evidenced by gas chromatography–mass spectrometry (GC-MS) results, as shown in Figure S1 in the Supporting Information. Hydrazine, NH_3, and H_2 are strong reducing agents, which would react with BCN at such high temperature under circulation system (Figure S2, Supporting Information) to produce DCN samples. To the best of our knowledge, this should be the first report on the utilization of photoenergy for the modification of g-C_3N_4.

The evolution of X-ray diffraction (XRD) patterns of the products obtained as a function of the current output is given

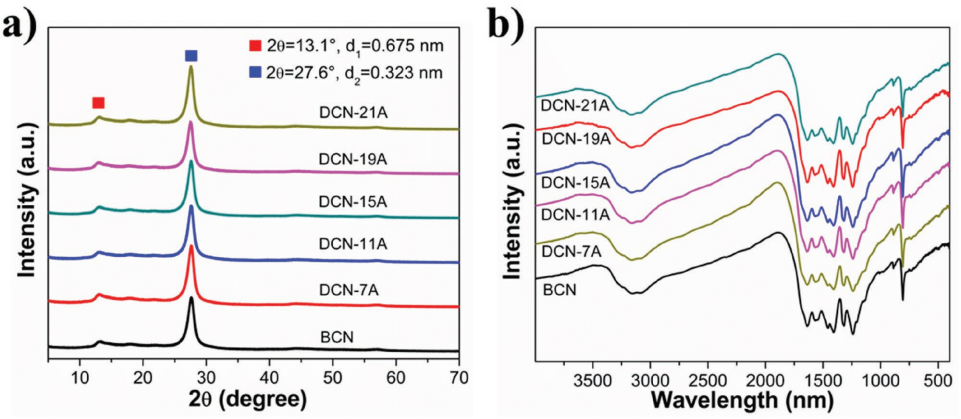

Figure 2. a) XRD patterns and b) FTIR spectra of BCN and DCN samples.

in **Figure 2**a. All the DCN samples show two typical diffraction peaks centered at 13.1° and 27.6°, which are consistent with the pristine BCN sample. Those two diffraction peaks of 13.1° and 27.6° are associated with the in-plane repeating units of the continuous heptazine framework and the stacking of the conjugated aromatic structure along *c*-axis of g-C_3N_4, respectively.[49] It indicates that the crystal structure of g-C_3N_4 is largely retained after the photothermal reduction process. Fourier transform infrared (FTIR) spectroscopy was used to further investigate the microstructure evolution of the g-C_3N_4. FTIR spectra (Figure 2b) also show no much change in the feature bands between 1900 and 700 cm^{-1} attributed to the trigonal $N(C)_3$/bridging $HN(C_2)$ units and heptazine ring of the melon unit.[50] This suggests that the original g-C_3N_4 backbone remains almost unchanged, which is inconsistent with the XRD results. The results of XRD patterns and FTIR spectra prove that the conjugated backbone structures of DCN are well maintained, which is essential for π-delocalized electronic systems to generate and transport photoexcited electron–hole pairs for the subsequent redox reactions.

In contrast to the unchanged crystal structure, the morphology of the g-C_3N_4 after photothermal reduction reaction is greatly changed, as demonstrated by the scanning electron microscopy (SEM) images in **Figure 3**. The pristine BCN sample displays the smooth surface; however, after photothermal treatment, the surfaces of resultant samples have been corroded and appear as irregular holey structures (Figure 3). The diameters of holes range from several nanometers to dozens of nanometers. The formation of holy structure should be from the hydrazine etching at high temperature, since no obvious morphology change is observed after photoassisted treatment without adding hydrazine (Figure S3, Supporting Information). The transmission electron microscopy (TEM) images, as shown in Figure S4 in the Supporting Information, further confirm that the DCN samples show holey structure, which are in good agreement with the SEM observation. The high angle annular dark field-scanning transmission electron microscopy (HAADF-STEM) image of DCN-15A further indicates its holey structure, and the corresponding elemental mapping images show that both C and N elements are homogeneously distributed in a holey way similar to the shape of the HAADF-STEM image (Figure S5, Supporting Information). Because of the formation of holey structure, DCN samples show the increased Brunauer-Emmett-Teller (BET) surface area and pore volume compared with pristine BCN (Figure S6 and Table S1, Supporting Information). Such a dramatically increased BET surface area and the formation of abundant holes in DCN could allow for exposing more active sites and facilitate the accessibility of reactants to the active surface, which should be more favorable for photocatalysis.[51,52]

The successful introduction of defects into g-C_3N_4 via photothermal treatment can be evidenced by X-ray photoelectron spectroscopy (XPS). High-resolution XPS spectra (Figures S7 and S8, Supporting Information) give similar C 1s and N 1s core electron peak regions of the carbon nitride products, indicating that this photothermal treatment has little influence on the C–N aromatic systems. The deconvolution of the overlapped N 1s peaks has produced three peaks centered at around 398.1, 398.8, and 400.2 eV, which can be ascribed to sp^2-hybridized aromatic nitrogen atoms bonded to carbon atoms (C=N−C), tertiary nitrogen (N−$(C)_3$) groups, and amino functional groups(C−N−H), respectively.[49] The elemental analysis manifests that the C/N atomic ratio gradually increases from 0.686 of BCN to 0.737 of DCN-21A (Table S2, Supporting Information), suggesting the preferential loss of N atoms during photothermal treatment. The C/N atomic ratio of DCN-21A sample becomes closer to the value of the stoichiometric carbon nitride (0.750). It is well known that the existence of residual amine groups is responsible for the higher concentration of nitrogen in the commonly available g-C_3N_4 than that in the stoichiometric one.[50] Moreover, it has been demonstrated that the loss of nitrogen in the amine groups was much easier than that in the N(sp^2) and N(sp^3) groups for g-C_3N_4.[43,50] Therefore, the increased C/N atomic ratio observed could be caused by the partial loss of the amine groups from the commonly available g-C_3N_4, which can be confirmed by the decreased peak area ratio and slightly increased binding energy of the amino functional groups (C−N−H) in the N 1s spectra of the carbon nitrides (Table S3, Supporting Information). This is also confirmed by the increased intensity of the 285.5 eV peak originating from the N=C bonding structure in the high resolution C 1s spectra of the carbon nitrides with the increase of current output (Figure S8 and Table S4, Supporting Information), which results from the defect-containing sp^2-bonded carbon atoms.[53,54] The measured H amount decreased from 2.27 wt%

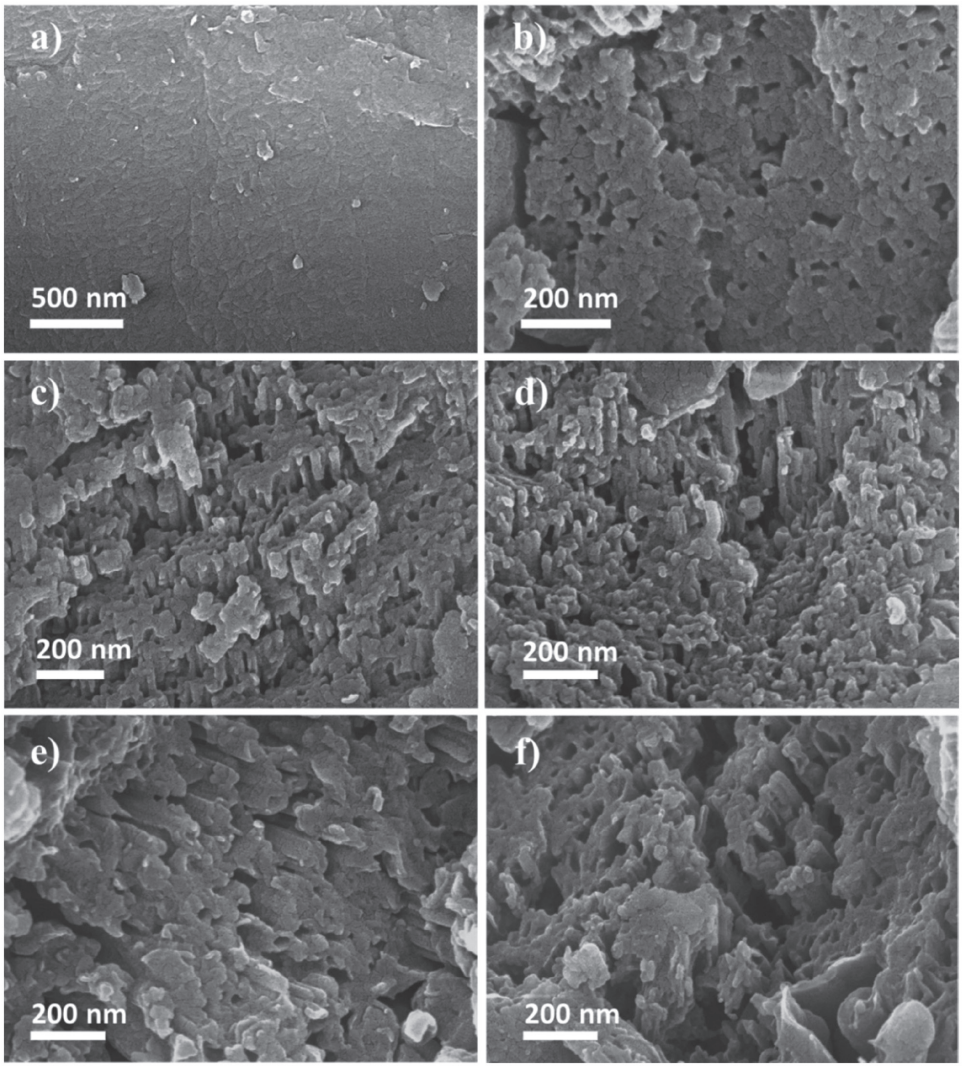

Figure 3. SEM images of a) BCN, b) DCN-7A, c) DCN-11A, d) DCN-15A, e) DCN-19A, and f) DCN-21A samples, respectively.

in BCN to 1.82 wt% in DCN-21A. The proposed schematic for the formation of this DCN by the photothermal treatment of BCN sample is illustrated in Figure S9 in the Supporting Information, and the BCN loses one NH_2 group to form nitrogen vacancies.

The above microstructure modification caused by nitrogen vacancies has a great influence on the electronic bandgap structure of g-C_3N_4, which can be evidenced by density functional theory (DFT) studies. As shown in **Figure 4**a,b, the calculated density of states of DCN shows an obvious decrease of intrinsic bandgap compared with BCN. Moreover, it can be seen that defect states appear below the CB of BCN in Figure 4b. The defect states can accommodate the electrons photoexcited from the valence band (VB) of BCN, which greatly contribute to the absorption of photons with energies smaller than the bandgap, promoting to more light harvesting. No defect states can be theoretically obtained if we use H substituting the N site (one NH_2 group is replaced by an H atom) as the model structure (Figure S10, Supporting Information), indicating that the simulated structure in Figure S9 in the Supporting Information is more reliable. Figure 4c shows the optical properties of BCN and all DCN samples, as measured by UV–vis absorption spectra. As expected, the absorption edges of the photothermally treated g-C_3N_4 samples display remarkable redshifts in comparison with the pristine bulk sample, which renders the narrowing of the intrinsic bandgaps. Consistent with these absorption results, the color of the powders suffers a matching variation from yellow to brown as the current output increases (insets in Figure 4c). The plots (Figure S11, Supporting Information) of the transformed Kubelka–Munk function versus the light energy show a gradual intrinsic bandgap narrowing from 2.75 eV of BCN to 2.55 eV of DCN-21A. The bandgap narrowing can be well explained as a consequence of the changed electronic structure caused by nitrogen vacancies, which is consistent with the DFT calculation results. To further investigate the influence of nitrogen vacancies on the relative positions of the conduction band minimum and valence band maximum of the samples, valence band X-ray photoelectron spectroscopy (VB-XPS) were employed to determine the electronic structure. The VB-XPS spectra show that the DCN samples have lower VB

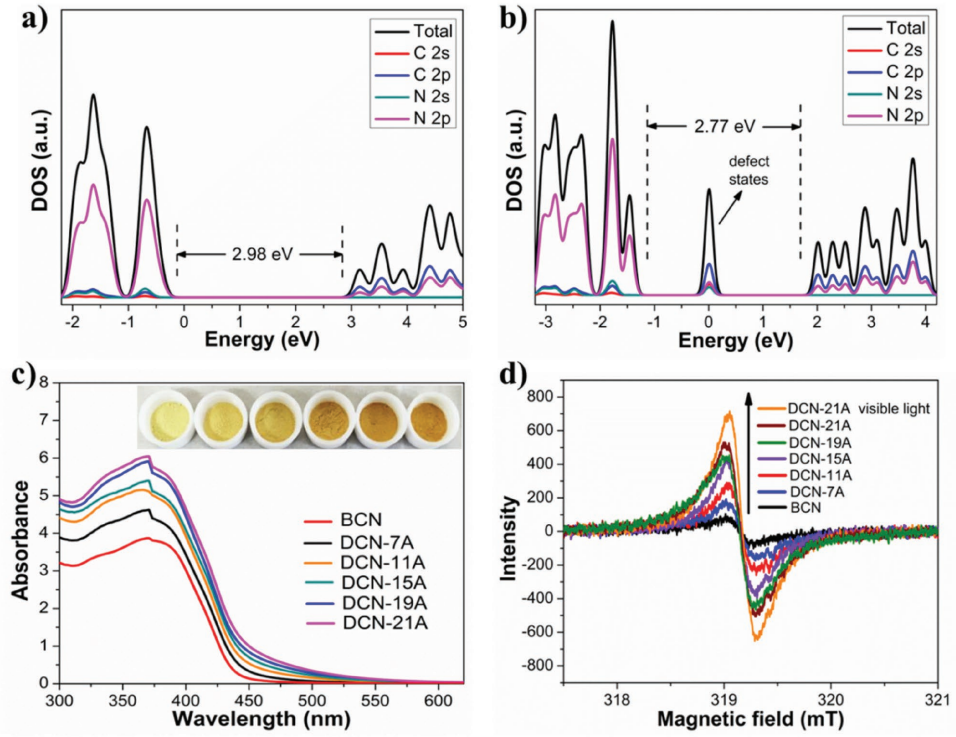

Figure 4. Density of states of a) BCN and b) DCN calculated from the model of Figure S8 in the Supporting Information. c) UV–vis absorption spectra and corresponding pictures of BCN and DCN samples, from left to right: BCN, DCN-7A, DCN-11A, DCN-15A, DCN-19A, and DCN-21A. d) ESR spectra of BCN and DCN samples.

edges than the BCN (Figure S12, Supporting Information). The CB position of BCN can be obtained by investigating the electrochemical Mott– plot (Figure S13, Supporting Information). The flat band potential of BCN is found to be at −1.17 V (vs normal hydrogen electrode (NHE), pH 7). Based on the differences in bandgaps and VB edges between the BCN and DCN, their band alignments are depicted in Figure S14, in the Supporting Information. The nature of the bandgap narrowing of the DCN is that nitrogen vacancies lead to the downshift of both the VB and the CB. The CB positions of DCN samples are still more negative than the reduction potential of O_2 to H_2O_2 (Figure S14, Supporting Information).[26]

To monitor the evolution of the electronic band structure for DCN with nitrogen vacancies, the room-temperature electron spin resonance (ESR) spectra were recorded. As shown in Figure 4d, all the samples exhibit an ESR signal with a g value of 2.003, which can be attributed to unpaired electrons on the sp^2-carbon atoms of the aromatic rings within π-bonded nanosized clusters.[49] Compared with pristine BCN, the gradually enhanced spin intensity of DCN samples gives evidence for the promoted formation of unpaired electrons after the introduction of nitrogen vacancies. This is probably due to the fact that the loss of nitrogen atoms would leave extra electrons, which are redistributed to their nearest carbon atoms delocalized among the big π-bonds of the g-C_3N_4, and thus lead to the formation of more unpaired electrons.[42] A slightly enhanced ESR signal under visible light illumination of DCN-21A provides the clue of promoted photochemical generation of radical pairs on its CB (Figure 4d), indicating that the photothermal treatment of g-C_3N_4 maintains its semiconducting properties.

Obviously, as shown in Figure 4c, broader and stronger absorption tails extending to 600 nm are also clearly observed for DCN samples. Usually, the absorption tail is attributed to the defect-related states located within the bandgap, which is consistent with the theoretical prediction (Figure 4b). Increasing the photothermal treatment temperature leads to a gradually increased band-tail-related absorption, indicating that higher density of defect states can be created at a higher temperature. The introduction of defect states leads to substantial suppression of radiative electron–hole recombination in carbon nitrides, as indicated by the greatly weakened photoluminescence (PL) peak in **Figure 5**a. For the pristine BCN, the spectrum shows a strong emission peak at 456 nm, which is originated from the band-to-band recombination of electrons and holes. The intensity of this band-to-band emission peak decreased dramatically upon the introduction of defect states, which means that the band-to-band recombination of electrons and holes was effectively inhibited. Moreover, the emission peak experiences a gradual redshift, which is attributed to the narrowing of bandgaps for DCN samples. To further reveal the photophysical characteristics of the photogenerated charge carriers, the time-resolved PL spectra were investigated and displayed in Figure 5b, which were monitored at the wavelength of the emission peak of each sample. By the triexponential fitting, the average lifetimes of the samples are calculated and presented in Figure 5b. The average PL lifetime gradually decreases from 15.85 ns in the pristine BCN to 5.04 ns in the

DCN-21A. The decreased lifetimes indicate that the depopulation of the excited states in the obtained DCN occurs more readily through nonradiative pathways, presumably by charge transfer of the electrons to some favorable defect states, e.g., surface states, and thus point to the improved charge transfer and separation.

The photocatalytic activities of the prepared samples were evaluated by H_2O_2 production from O_2 reduction. The photocatalytic reactions were performed with isopropanol (IPA) as electron and proton donor, and the setup of the experiment was shown in Figure S15 in the Supporting Information. An IPA/water mixture containing g-C_3N_4 photocatalyst was photoirradiated by simulated sunlight with an L-42 cutoff filter (AM1.5, $\lambda > 420$ nm) under stirring and O_2-equilibrated conditions. The H_2O_2 is produced via a two-electron reduction of O_2, and the reaction equations can be described as follows[25]

$$CH_3CHOHCH_3 + 2h^+ \rightarrow CH_3COCH_3 + 2H^+ \quad (1)$$

$$O_2 + 2H^+ + 2e^- \rightarrow H_2O_2 \quad (2)$$

The generated H_2O_2 can be monitored via *N*,*N*-diethyl-*p*-phenylenediamine (DPD)–horseradish peroxidase (POD) method (see more details in Experimental Section). The time-dependent absorption spectra of the DPD/POD solution with different photocatalysts were shown in Figure S16 in the Supporting Information. The concentration of H_2O_2 can be monitored by the absorption intensity of the solution at 551 nm, which can be calculated through the prepared standard curves (Figure S17, Supporting Information). **Figure 6**a shows the time-dependent evolution of H_2O_2 produced by BCN and DCN samples. The concentration of H_2O_2 increases almost linearly as irradiation time prolongs, indicating that all the samples are able to produce H_2O_2 in the photocatalytic reaction system. The production of H_2O_2 was negligible in a control experiment when O_2 was replaced by Ar in the photocatalytic reaction, indicating that H_2O_2 was indeed generated from photocatalytic O_2 reduction. All the DCN samples show a much superior activity to the pristine BCN sample. The photocatalytic H_2O_2 production rate of the samples increases with increasing current output up to 15 A. Further increasing the current output to 19 or 21 A gives rise to a gradually decreased activity but they are still superior to the pristine sample. The reason for this trend will be discussed later. After photocatalytic reaction for 2.5 h, about 12.1 μmol H_2O_2 was produced over DCN-15A, which is 10.1 times higher than that of the pristine BCN. DCN-15A shows higher photocatalytic activity for H_2O_2 production than some reported g-C_3N_4-based photocatalysts (Table S5, Supporting Information). Moreover, DCN-15A also shows higher activity than graphitic carbon nitride nanosheet, H_3PO_4 protonated porous graphitic carbon nitride nanosheet, and DCN under the same reaction conditions (see more details in Figures S18 and S19, Supporting Information), which indicates that the introduction of nitrogen vacancies via photothermal treatment should represent an effective approach to improve the photocatalytic H_2O_2 production activity for g-C_3N_4-related photocatalysts.

The wavelength-dependent apparent quantum efficiency (AQE) of H_2O_2 production was then further investigated to prove whether or not the reaction proceeds through light absorption. Figure 6c shows the UV–vis diffuse reflectance spectra of the DCN-15A along with the AQE of H_2O_2 evolution as a function of the incident light wavelength. The trend of AQE almost agrees with the absorption spectrum of DCN-15A, indicating that photoexcitation of DCN-15A promotes H_2O_2 formation. The photocatalytic stability of this sample was evaluated by collecting and reusing the DCN-15A for three times. As shown in Figure 6d, the DCN-15A can retain its good photocatalytic activity after three cycles of reaction. XRD patterns were further employed to characterize the recovered catalyst after the third cycling reactions (Figure S20, Supporting Information). As expected, any obvious changes in structure were not observed, again supporting the robust nature of DCN-15A.

The above information clearly shows the advantages of the photothermal-treated g-C_3N_4 for photocatalytic H_2O_2 production. We are now in a position to try to understand the mechanisms behind the functions. The photocatalytic efficiency of a photocatalyst is usually determined by the synergistic effects of three basic steps of photocatalysis, (i) light absorption ability, (ii) charge separation efficiency, and (iii) surface transfer of photogenerated charge carriers.[50] On the one hand, the higher BET surface area combined with the unique holey structure provides DCN samples with more exposed active catalytic sites and channels, which play an important role in shortening the diffusion lengths of both the photoexcited electrons from the interior to edges of the holes and reactants from the surface to

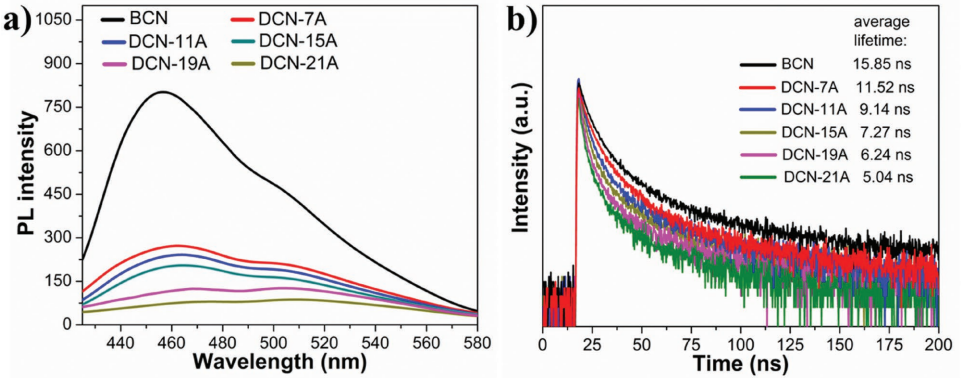

Figure 5. a) PL spectra and b) decay time spectra of BCN and DCN samples.

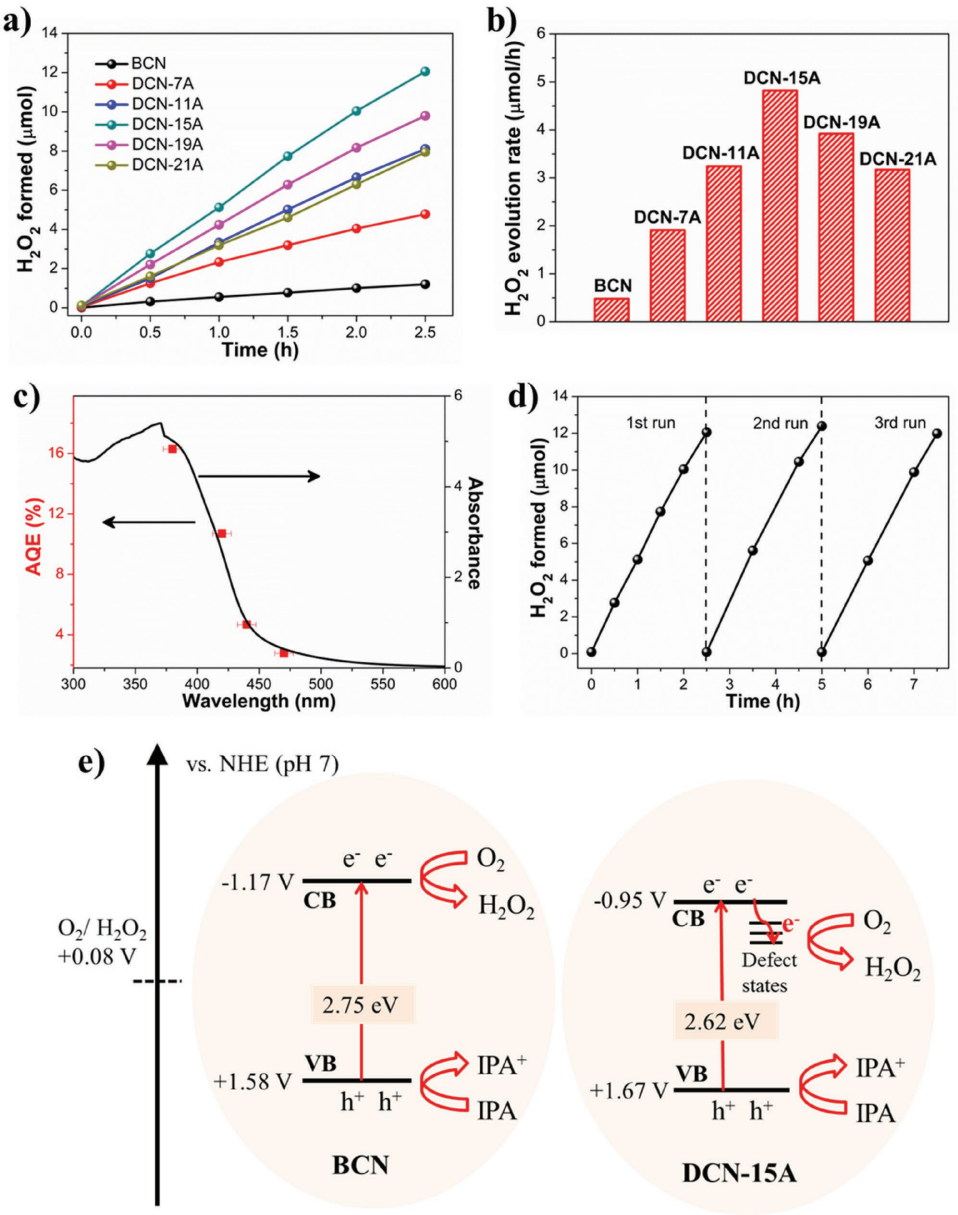

Figure 6. a) Time-dependent evolution of H_2O_2 produced by BCN and DCN samples. b) photocatalytic H_2O_2 activity comparison of different samples. c) UV–vis absorbance spectrum and wavelength-dependent AQE of DCN-15A. d) Recycling test of DCN-15A. e) Schematic of mechanisms underlying the photoexcited dynamics involved in photocatalytic H_2O_2 evolution over BCN and DCN-15A.

the interior of g-C_3N_4 particle along interconnected holes. These structure-induced favorable features can lower the bulk recombination probability of electrons and holes, and also promote mass transport in DCN, definitely favoring the proceeding of photocatalytic reactions. On the other hand, the introduction of nitrogen vacancies via photothermal reduction reaction can extend visible-light absorption range to increase the low-energy photon excitations, whose origin is the decreased intrinsic bandgap and the formation of defect states. The introduction of defect states in DCN suppresses the radiative electron–hole pairs recombination as demonstrated by Figure 5, which is due to the CB-to-defect states charge transfer processes induced by the increased defects/localized states within the bandgaps (Figure 6e), thus point to the improved charge separation. These electronic structure-induced favorable features also favor the proceeding of photocatalytic reactions. However, the introduction of nitrogen vacancies would also induce the downshift of CB positions and defect states (Figure S21, Supporting Information), which would decrease the reductive ability of photogenerated electrons, exerting a negative effect on the photocatalytic H_2O_2 production. Moreover, the overformation of bulk defects beyond 15 A could serve as recombination centers for electrons and holes. Those two main reasons can explain why the photocatalytic activities decrease beyond 15 A.

3. Conclusion

In summary, holey DCN was successfully constructed via a facile photoassisted heating process. The obtained DCN products possess not only tunable electronic structures controlled by nitrogen vacancies, but also holey structure with abundant holes formed throughout the whole particles. The narrowed bandgap and the rationally created defect states enable DCN to harvest visible light and suppress radiative electron–hole recombination more efficiently than pristine BCN. In addition, the abundant holes can provide DCN more reductive reaction sites and facilitate the accessibility of reactants to the active surface. As a consequence of these favorable features, the DCN with an optimized nitrogen vacancies introduction gives a significantly enhanced photocatalytic H_2O_2 production activity under visible light. It is expected that the simple and highly effective strategy adopted here could be extended to modify other materials for improved solar energy capture and conversion.

4. Experimental Section

Preparation of the Photocatalysts: BCN was prepared by heating dicyandiamide (Wako Co.) in a covered crucible to 550 °C for 4 h in air at a heating rate of 5 °C min^{-1}. DCN was prepared by photoassisted treatment of BCN with hydrazine in a batch-type reaction system with a total volume of about 330 mL (Figure S2, Supporting Information). In brief, 0.2 g BCN powder was dispersed on a porous quartzose film in the reaction cell, followed by injecting 3 mL hydrazine solution. The reaction system was evacuated for a few minutes to remove air completely (no N_2 and O_2 could be detected), and then was heated by a 300 W Xe lamp with adjustable current output (from 7 to 21 A) for 30 min. After photoassisted treatment, the obtained DCN samples were cooled down to room temperature and collected by washing with water for several times, and dried under vacuum at 60 °C.

Characterization: The XRD patterns of the prepared photocatalysts were measured by powder XRD on an X'Pert PRO diffractometer (PANalytical). The UV–vis spectra of the photocatalysts powder were obtained on a UV–visible spectrophotometer (SHIMADZU UV-2600) and $BaSO_4$ was used as the reflectance standard reference. The SEM images of the as-prepared photocatalysts were taken on a scanning electron microscope (S4800, Hitachi Co., Japan). TEM, HAADF-STEM and elemental mapping images were taken on a transmission electron microscope (2100F, JEOL Co., Japan). Nitrogen adsorption–desorption isotherms and BET surface area were recorded using a BEL SORP-mini II (BEL Japan INC., Japan) at 77 K. The PL spectra were recorded by using JASCO FP-6500 spectrofluorometer, and the excitation wavelength was 370 nm. The decay time measurements were carried out on a compact fluorescence lifetime spectrometer (Quantaurus-Tau, C11367, HAMAMATSU), and an LED lamp (365 nm) was used as an excitation source. XPS (PHI Quantera SXM, ULVAC-PHI Inc., Japan) was used to analyze the compositions and chemical state of the samples. The FTIR spectra of the samples were studied by Thermoscientific Nicolet 4700. The ESR measurements were carried out with JEOL JES-FA-200 at room temperature in the air.

DFT Calculations: All calculations here were performed with the Vienna ab-initio Simulation Package based on the DFT. The Projector-augmented wave with generalized gradient approximation (GGA)-PBE function was used for the electron–ion interactions. The number of *k* points and the cutoff energy were increased until the calculated total energy converged within an error of 1×10^{-5} eV $atom^{-1}$. Therefore, a cutoff energy of 500 eV with $3 \times 3 \times 1$ k points was set for the slab model with a 14 Å thickness of vacuum layer. The energy convergence tolerance was set to below 1×10^{-5} eV $atom^{-1}$. The lattice and atomic coordinates were relaxed until the Hellmann–Feynman force on each atom was reduced to less than 0.01 eV $Å^{-1}$.

Photocatalytic Experiments: The photocatalytic H_2O_2 production reactions were carried out with 50 mg photocatalyst suspending in an O_2-equilibrated aqueous solution (60 mL solution containing 20 vol% IPA as a sacrificial electron donor) in a glass reaction cell (Figure S15, Supporting Information). A simulated sunlight with an L-42 cutoff filter (AM1.5, $\lambda > 420$ nm) was used as the visible light source. The evolved amount of H_2O_2 was measured by using the colorimetric DPD method. The DPD method is based on the oxidation of *N*,*N*-diethyl-*p*-phenylenediamine (DPD) catalyzed with horseradish peroxides (POD) by H_2O_2. Briefly, 0.1 g of DPD was dissolved in 10 mL 0.05 M H_2SO4, denoted as solution A. 10 mg of peroxidase (POD) was dissolved in 10 mL water, denoted as solution B. 10 mL of 0.1 M Na_2HPO_4 solution and 90 mL of 0.1 M NaH_2PO_4 solution were mixed together to obtain solution C. Then 3 mL deionized water, 0.3 mL solution C, 30 µL solution A and 30 µL solution B were mixed together to obtain solution D. The time-dependent H_2O_2 generation was measured as follows: 1 mL filtration from reaction solution was dispersed into solution D, which was monitored by the absorption of the solution at 551 nm and determined with UV–vis spectrophotometer. The AQE was measured by using an AM1.5 lamp combined with wavelength-dependent band-pass filters (MIF-W, Optical Coatings Japan Co., Japan). A radiant power energy meter (Ushio Spectroradiometer, USR-40) was applied to measure the number of incident photons. The AQE was calculated according to the following equations

$$\mathrm{AQE}\ (\%) = \frac{\text{number of reacted electrons}}{\text{number of incident photons}} \times 100\% = \frac{\text{number of evolved hydrogen peroxide molecules} \times 2}{\text{number of incudent photons}} \times 100\% \quad (3)$$

Supporting Information

Supporting Information is available from the Wiley Online Library or from the author.

Acknowledgements

This work received financial support from the World Premier International Research Center Initiative (WPI Initiative) on Materials Nano-architectonics (MANA), MEXT (Japan), the National Basic Research Program of China (973 Program, 2014CB239301), and the National Natural Science Foundation of China (21633004).

Conflict of Interest

The authors declare no conflict of interest.

Keywords

g-C3N4, nitrogen defects, photocatalyst, photoassisted

Received: September 11, 2017
Revised: November 27, 2017
Published online:

[1] S. Kato, J. U. Jung, T. Suenobu, S. Fukuzumi, *Energy Environ. Sci.* **2013**, *6*, 3756.
[2] R. S. Disselkamp, *Int. J. Hydrogen Energy* **2010**, *35*, 1049.
[3] M. Teranishi, S. Naya, H. Tada, *J. Am. Chem. Soc.* **2010**, *132*, 7850.

[4] V. Maurino, C. Minero, G. Mariella, E. Pelizzetti, *Chem. Commun.* **2005**, *20*, 2627.
[5] Y. Isaka, K. Oyama, Y. Yamada, T. Suenobu, S. Fukuzumi, *Catal. Sci. Technol.* **2016**, *6*, 681.
[6] L. Shi, P. Li, W. Zhou, T. Wang, K. Chang, H. Zhang, T. Kako, G. Liu, J. Ye, *Nano Energy* **2016**, *28*, 158.
[7] H. Hayashi, S. Katayama, T. Komura, Y. Hinuma, T. Yokoyama, K. Mibu, F. Oba, I. Tanaka, *Adv. Sci.* **2017**, *4*, 1600246.
[8] L. Shi, T. Wang, H. Zhang, K. Chang, X. Meng, H. Liu, J. Ye, *Adv. Sci.* **2015**, *2*, 1500006.
[9] X. Wang, K. Maeda, A. Thomas, K. Takanabe, G. Xin, J. M. Carlsson, K. Domen, M. Antonietti, *Nat. Mater.* **2009**, *8*, 76.
[10] Y. Zheng, L. Lin, B. Wang, X. Wang, *Angew. Chem,. Int. Ed.* **2015**, *54*, 12868.
[11] G. Zhang, C. Huang, X. Wang, *Small* **2015**, *11*, 1215.
[12] W.-J. Ong, L.-L. Tan, Y. H. Ng, S.-T. Yong, S.-P. Chai, *Chem. Rev.* **2016**, *116*, 7159.
[13] S. Cao, J. Low, J. Yu, M. Jaroniec, *Adv. Mater.* **2015**, *27*, 2150.
[14] L. Sun, M. Yang, J. Huang, D. Yu, W. Hong, X. Chen, *Adv. Funct. Mater.* **2016**, *26*, 4943.
[15] V. W.-H. Lau, V. W.-Z. Yu, F. Ehrat, T. Botari, I. Moudrakovski, T. Simon, V. Duppel, E. Medina, J. K. Stolarczyk, J. Feldmann, V. Blum, B. V. Lotsch, *Adv. Energy Mater.* **2017**, *7*, 1602251.
[16] K. Schwinghammer, M. B. Mesch, V. Duppel, C. Ziegler, J. Senker, B. V. Lotsch, *J. Am. Chem. Soc.* **2014**, *136*, 1730.
[17] J. Liu, Y. Liu, N. Liu, Y. Han, X. Zhang, H. Huang, Y. Lifshitz, S. T. Lee, J. Zhong, Z. Kang, *Science* **2015**, *347*, 970.
[18] Y. Kang, Y. Yang, L.-C. Yin, X. Kang, G. Liu, H.-M. Cheng, *Adv. Mater.* **2015**, *27*, 4572.
[19] Q. Liang, Z. Li, Z.-H. Huang, F. Kang, Q.-H. Yang, *Adv. Funct. Mater.* **2015**, *25*, 6885.
[20] G. Zhang, S. Zang, X. Wang, *ACS Catal.* **2015**, *5*, 941.
[21] L. Shi, K. Chang, H. Zhang, X. Hai, L. Yang, T. Wang, J. Ye, *Small* **2016**, *12*, 4431.
[22] H. Zhang, L. Zhao, F. Geng, L.-H. Guo, B. Wan, Y. Yang, *Appl. Catal., B* **2016**, *180*, 656.
[23] L. Shi, T. Wang, H. Zhang, K. Chang, J. Ye, *Adv. Funct. Mater.* **2015**, *25*, 5360.
[24] P. Xia, B. Zhu, J. Yu, S. Cao, M. Jaroniec, *J. Mater. Chem. A* **2017**, *5*, 3230.
[25] Y. Shiraishi, S. Kanazawa, Y. Sugano, D. Tsukamoto, H. Sakamoto, S. Ichikawa, T. Hirai, *ACS Catal.* **2014**, *4*, 774.
[26] Y. Shiraishi, S. Kanazawa, Y. Kofuji, H. Sakamoto, S. Ichikawa, S. Tanaka, T. Hirai, *Angew. Chem., Int. Ed.* **2014**, *53*, 13454.
[27] Y. Kofuji, Y. Isobe, Y. Shiraishi, H. Sakamoto, S. Tanaka, S. Ichikawa, T. Hirai, *J. Am. Chem. Soc.* **2016**, *138*, 10019.
[28] G. -H. Moon, M. Fujitsuka, S. Kim, T. Majima, X. Wang, W. Choi, *ACS Catal.* **2017**, *7*, 2886.
[29] Q. Han, B. Wang, J. Gao, Z. Cheng, Y. Zhao, Z. Zhang, L. Qu, *ACS Nano* **2016**, *10*, 2745.
[30] S. Guo, Z. Deng, M. Li, B. Jiang, C. Tian, Q. Pan, H. Fu, *Angew. Chem., Int. Ed.* **2016**, *55*, 1830.
[31] J. Ran, T. Y. Ma, G. Gao, X.-W. Du, S. Z. Qiao, *Energy Environ. Sci.* **2015**, *8*, 3708.
[32] X. Lu, K. Xu, P. Chen, K. Jia, S. Liu, C. Wu, *J. Mater. Chem. A* **2014**, *2*, 18924.
[33] J. Zhang, M. Zhang, C. Yang, X. Wang, *Adv. Mater.* **2014**, *26*, 4121.
[34] X. She, J. Wu, J. Zhong, H. Xu, Y. Yang, R. Vajtai, J. Lou, Y. Liu, D. Du, H. Li, P. M. Ajayan, *Nano Energy* **2016**, *27*, 138.
[35] J. Sun, J. Zhang, M. Zhang, M. Antonietti, X. Fu, X. Wang, *Nat. Commun.* **2012**, *3*, 1139.
[36] J. Xu, Y. Li, S. Peng, G. Lu, S. Li, *Phys. Chem. Chem. Phys.* **2013**, *15*, 7657.
[37] J. Qin, J. Huo, P. Zhang, J. Zeng, T. Wang, H. Zeng, *Nanoscale* **2016**, *8*, 2249.
[38] C. Li, S. Wang, T. Wang, Y. Wei, P. Zhang, J. Gong, *Small* **2014**, *10*, 2783.
[39] L. Yao, D. Wei, Y. Ni, D. Yan, C. Hu, *Nano Energy* **2016**, *26*, 248.
[40] A. Zada, M. Humayun, F. Raziq, X. Zhang, Y. Qu, L. Bai, C. Qin, L. Jing, H. Fu, *Adv. Energy Mater.* **2016**, *6*, 1601190.
[41] C. Li, Y. Du, D. Wang, S. Yin, W. Tu, Z. Chen, M. Kraft, G. Chen, R. Xu, *Adv. Funct. Mater.* **2017**, *27*, 1604328.
[42] P. Niu, G. Liu, H.-M. Cheng, *J. Phys. Chem. C* **2012**, *116*, 11013.
[43] P. Niu, L. Yin, Y. Yang, G. Liu, H.-M. Cheng, *Adv. Mater.* **2014**, *26*, 8046.
[44] G. Dong, W. Ho, C. Wang, *J. Mater. Chem. A* **2015**, *3*, 23435.
[45] H. Yu, R. Shi, Y. Zhao, T. Bian, Y. Zhao, C. Zhou, G. I. N. Waterhouse, L.-Z. Wu, C.-H. Tung, T. Zhang, *Adv. Mater.* **2017**, *29*, 1605148.
[46] Z. Hong, B. Shen, Y. Chen, B. Lin, B. Gao, *J. Mater. Chem. A* **2013**, *1*, 11754.
[47] Y. Guo, J. Li, Y. Yuan, L. Li, M. Zhang, C. Zhou, Z. Lin, *Angew. Chem., Int. Ed.* **2016**, *55*, 14693.
[48] G. Liu, X. Meng, H. Zhang, G. Zhao, H. Pang, T. Wang, P. Li, T. Kako, J. Ye, *Angew. Chem., Int. Ed.* **2017**, *56*, 5570.
[49] L. Yang, J. Huang, L. Shi, L. Cao, Q. Yu, Y. Jie, J. Fei, H. Ouyang, J. Ye, *Appl. Catal., B* **2017**, *204*, 335.
[50] Y. Kang, Y. Yang, L. Yin, X. Kang, L. Wang, G. Liu, H.-M. Cheng, *Adv. Mater.* **2016**, *28*, 6471.
[51] L. Mei, H. Zhao, B. Lu, *Adv. Sci.* **2015**, *2*, 1500116.
[52] R. C. Pawar, S. Kang, J. H. Park, J.-H. Kim, S. Ahn, C. S. Lee, *Sci. Rep.* **2016**, *6*, 31147.
[53] W.-J. Ong, L.-L. Tan, S.-P. Chai, S.-T. Yong, *Dalton Trans.* **2015**, *44*, 1249.
[54] C. Chang, Y. Fu, M. Hu, C. Wang, G. Shan, L. Zhu, *Appl. Catal., B* **2013**, *142*, 553.

